2012 12th International Conference on Control, Automation, Robotics & Vision
Guangzhou, China, 5-7th December 2012 (ICARCV 2012)

Th34.5

Remission based Improvement of Extrinsic Parameter Calibration of Camera and Laser Scanner

Stefan Krause and Robert Evert
German Aerospace Center, Institute of Flight Systems
38108 Braunschweig, Germany
Email: stefan.krause@dlr.de

Abstract—**This paper presents an improvement for an automatic extrinsic parameter calculation between a monocular camera and single line laser range finder. The focus of this work is a further reduction of calibration errors compared to other existing methods, and the unique and automatic identification and detection of a calibration object under usage of the remission measurements of the laser scanner data. The use of the remission measurements leads to a reduction of the edge effect, which leads to error measurements at the edges of a measured object, if distance measurements are used exclusively. Further, the usage of the remission measurements enables the unique identification of a new calibration object with a significant remission signature. The result is an automatic extrinsic parameter calculation which works reliably with a high accuracy. The performance of the proposed method was verified in simulation and experiments. In order to classify the results of simulation and experiments, they were compared to other existing methods.**

I. INTRODUCTION

In the robotic and unmanned aircraft research, laser range finders (LRF) and cameras are widely used in single or combined applications to enable mapping, navigation, or obstacle avoidance. The unmanned aircraft (UAV), which was used by by us, the German Aerospace Center Braunschweig, is the maxiARTIS. It can be seen in Figure 1 equipped with stereo camera and single line LRF.

Fig. 1: The maxiARTIS UAV equipped with stereo camera and single line LRF.

Both sensors have advantages and disadvantages, which makes them convenient for different tasks or environments (indoor/ outdoor). A LRF can directly measure the 3D coordinates of a point in the environment. Further, the technology is independent of external illumination. A disadvantage of LRF devices is, that it is difficult, if not impossible, to detect patterns onto planar surfaces or different colors.

For a camera, it is difficult to measure directly 3D structures except of stereo applications with more cameras or different points of view. Further, it is a passive sensor, and so it is dependent from external illumination. However, cameras allow an easy acquirement of colors, pattern, etc.

In order to overcome of the individual sensors' disadvantages, a fusion of these complementary sensors is beneficial. A possible combination can generate a joint field of view, which enables the acquisition of more precise data or a more detailed data set (colored/textured 3D structures) [3], [12], [13].

In order to fuse the data sources in a cooperative data collection, it is necessary to transfer the measurements of both sensors into one reference frame system. Therefore, the poses (extrinsic parameters, translation and rotation) of both sensors towards each other, in the reference frame system, must be known. The determination of the corresponding sensor poses in a joint coordination system was shown in different approaches based on different sensor hardware specification.

A. Related Work

The approaches, suggested by [4], [8], [11], [15], use a LRF with visible beams in combination with a color camera. The crucial step of these approaches was the localization of the laser spots in the camera images and the computation of the transformation from the camera pose to the LRF pose. A disadvantage of this approach is that the laser changes the environment awareness of the camera. The laser dots generate e.g. red points, and thus it can impede the camera perception of other colors or pattern.

Other approaches use 3D LRF in association with stereo cameras [2], [6], [16]. Thereby, two 3D images were generated to match extracted features in order to get accordances and calculate the extrinsic sensor parameter. The disadvantage of this approach is that 3D LRFs are currently expensive and bulky. Therefore, these devices are not usable in most robotic or unmanned aircraft applications.

Further approaches [10], [14], [18] are based on the operation of 2D single line LRF, which are increasingly used in different research fields. These systems often use invisible beams, which are e.g. in the near-infrared band and therefore prevent the localization in the camera image, except when used infrared cameras. The approaches presented by Zhang and Pless [18] and Li et al. [10] use a 2D LRF in combination with a monocular camera to detect a planar calibration object. Both

approaches work sufficiently. However, both methods work only manually. The identification of the calibration object in the single data set requires interactions of a user.

Another point is the assumption that the distance LRF measurements depict a correct image of the environment, except minor inaccuracies in the distance values [10], [18]. However, this assumption in our opinion is not correct. Boehler [5] shows that the reflectivity of the spotted object surface can influence the distance measuring and therefore the dimensions of the object in the LRF data set. One phenomenon, which [5] describes, is the edge effect. Against a mathematic ray, a real laser spot has a divergence. Therefore, it is possible, that only a part of a spot hits an object surface. The rest of the spot may be reflected from the adjacent surface, a different surface behind the edge, or not at all (when no further object is present within the possible range of the scanner). The result is that the scanner possibly detects more than one distance for one emitted spot and produces a variety of wrong points in the vicinity of edges.

B. Problem Definition

An automatic calibration of a device with a calibration object requires that the calibration object can be uniquely identified by that device. In the presented work, these devices are a single-line LRF and a monocular gray scaled camera.

The works of [10], [18] use a planar calibration object, which is represented in the single-line LRF data only by a line. The line or especially its length cannot be used for a unique identification of an object, because the line length depends on the position and orientation of the object against the LRF. Therefore, lines are possible, which have the length of one beam diameter up to the largest dimension of the measured object. The approaches in [10], [18] solve this problem by using manual identification in combination with an approximately known position of the calibration object in front of the LRF.

The identification of the calibration object in the camera image is not as difficult as in the LRF data. However, in the works of [10], [18] it was also done manually which is time-consuming and error-prone, too.

Several pre-tests with the LRF showed that the distance data does not depict the measured objects correctly. The object dimension in the LRF data set is larger than in real. A probably source of the deviation is the edge effect [5]. The edge effect leads to the situation that more than one echo from different distances arrive at the LRF if a spot hits an edge. The internal handling of the LRF, how multiple received echoes are handled, leads to different distances in resultant measurements. Examples of the internal handling are, that the average of all echoes, or only the first echo is used. The chosen LRF uses, identified by experiments, a first echo handling, which only uses the first echo without considering the subsequent echoes. Therefore, all LRF beams, which at first hit the test object and their resultant echoes being detected by the LRF, lead to distance values of the test object. The measurement result is independent of the beam profile part which hits the test object.

This behavior leads to the situation that edge hits cannot be identified in a LRF distance scan. Therefore, the aim is to identify the measurements which are influenced by the edge effect and to find a solution to reduce this influence.

II. Calibration Object Design

The proposed calibration uses line features as proposed by [10] and identifies intersections between them. The intersections are the basis for the extrinsic parameter estimation. Therefore, the calibration object is equipped with lines and edges which can be detected by the camera as well as by the LRF. The result is that both data sets contain corresponding measurements which must be brought one above the other.

Beside the distance measurement, some LRFs are able to measure the remission of each scan point [7], [9], [17]. The remission denotes the diffuse reflection of light waves on surfaces. The magnitude of the remission depends on surface's roughness, color and material. This ability is the base of the newly developed approach. Therefore, a calibration object was equipped with 3M Scotchlite reflection foil which has a significant remission signature in an office or laboratory environment. The foil increases the remission values way above a level which can be achieved in standard indoor or outdoor environments [1]. The remission of the foil, in comparison to other materials, can be seen in table I. The new

material/ color	remission value
black painted wood	≈ 1800
brown cardboard	≈ 2400
white painted wood	≈ 2900
reflector strip	≈ 14500

TABLE I: Remission measurement values of different test objects in 3 m range to a Hokuyo UTM-30LX [9].

calibration object bases also on a black isosceles rectangular triangle [10] with a hypotenuse of 0.7 m. Both catheti of the black triangle center are taped with 2 mm thin striped reflection tape. The stripes were positioned at the inner edge of the black triangle. The reflecting foil is colored dark blue, and so it is hardly distinguished from the black triangle background by a monochrome gray scaled camera. In the center of the black triangle there is a chess board pattern which can be used for the intrinsic calibration of the camera. In the current implementation, this is used for a better identification of the calibration object. Figure 2 shows the calibration object. The reflection foil stripes are marked in this figure with white crossing lines to enable a better identification. At the real calibration object, the strips cannot be visually detected, as can be seen later in Figure 8.

III. Calibration Procedures

The aim of extrinsic calibration parameters' computation is to calculate the rotation $\phi(\theta_x, \theta_y, \theta_z)$ and translation $t(t_x, t_y, t_z)$ of the LRF to the camera.

The identification and detection of the calibration object starts with the detection of the interior black triangle by the camera. The analysis of the data is accomplished with an open image
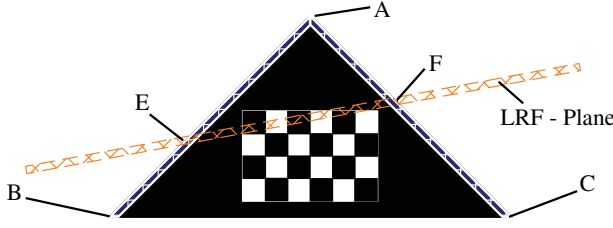
Fig. 2: Calibration Object

processing library (OpenCV). The results are the three corners A (top), B (left wing) and C (right wing), as is seen in Figure 2. The coordinates of the triangle corners were calculated with sub-pixel accuracy.

The LRF returns a distance and remission image of the environment. An example LRF data set of the calibration object can be seen in Figure 3, which shows the two remission peaks generated by the reflection foil R_0 and R_1 and the distance measurements with the edges of the calibration object D_1 and D_0. The distance measurements are given in polar coordinates with an angle φ and a range r. During the work with the remission measurements, it became clear that the remission measurements can be also an indicator for the edge effect. Based on this insight, the distance measurements $D_0(\varphi_{D_0}, r_{D_0})$ and $D_1(\varphi_{D_1}, r_{D_1})$ were not used further to survey the calibration object.
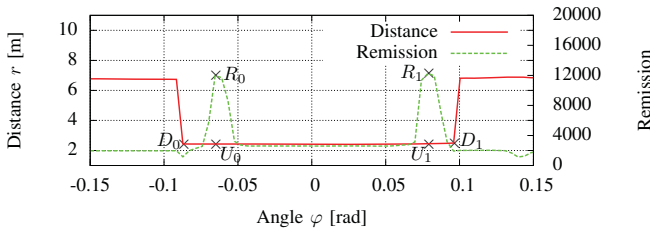

Fig. 3: Survey of a calibration object with distance and remission measurements.

In the remission image, the two peaks R_0 and R_1 of the reflective foil are searched. Subsequently, the distance data between the angles φ_{R_0} and φ_{R_1} are used to compute a regression line $g_{reg} : \vec{m} = \vec{m_0} + \vec{n} * \lambda$ (line vector equation) by using a principal component analysis. The use of a regression line to calculate E and F leads to a reducing influence of noise and outliers in comparison to the exclusive use of the distance measurements, which are at the same angle as φ_{R_0} and φ_{R_1}. After this, the intersections between the line g_{reg} and the normals, which contain both points $U_0 = (\varphi_{R_0}, r_{D_{\varphi_{R_0}}})$ and $U_1 = (\varphi_{R_1}, r_{D_{\varphi_{R_1}}})$, are determined. The intersection coordinates are the points E (left) and F (right), as is seen in Figure 2. The computation is shown in the example with the points $\vec{u_0}$ (Cartesian representation of the polar coordinates U_0) and E in equation 1. The calculation of F is analog.

$$E = \vec{m_0} + \vec{n} * \left(\frac{\vec{n} * (\vec{u_0} - \vec{m_0})}{\vec{n}^2} \right) \qquad (1)$$

The camera coordinate frame is the joint reference frame. Assume that the camera is a pinhole camera and the images are rectified, the points A, B and C, which are in the camera reference frame, can be projected onto the points a, b and c onto the camera image plane by the equations presented in [19]. Under usage of the initial parameters of ϕ and t, also the points E and F can be transformed from the laser frame in the camera frame and finally onto e and f on the camera plane.

The points a and b can be understood as points of a line, and if the calibration is correct e should be a further point of this line. The same takes effect for the points a and c in combination with the point f. Therefore, the aim is to estimate the parameter ϕ and t in a manner, that the distances between the respective lines $\vec{ab}$ ($\vec{ac}$) and points $\vec{e}$ ($\vec{f}$) are minimal. The distance $d(ab, e)$ between the line $\vec{ab}$ and the point $\vec{e}$ can be calculated with equation 2.

$$d(ab, e) = \frac{\|\vec{eb} \times \vec{ab}\|}{\|\vec{ab}\|} \qquad (2)$$

In order to solve the six-dimensional problem, minimal six snap shots of the calibration object stage are needed. The snapshots (indexed i) should have different positions, orientations and distances of the calibration object in the field of view (FoV) of the camera and the LRF. The problem to find the optimal parameter ϕ and t can be formalized as minimizing the sum of both distances $d(ab, e)$ and $d(ac, f)$, as shown in equation 3. This calculation is a nonlinear optimization problem which is solved with a Levenberg-Marquardt approach.

$$min \left\{ \sum_i [d(a_i b_i, e_i) + d(a_i c_i, f_i)]^2 \right\} \qquad (3)$$

Based on the results which were generated during the work with the proposed approach, and the results presented by [10], [18], it is recommended that more than 25 snapshots are recorded. For the recording of the calibration object, it is recommended that it is recorded in different positions, which are chosen uniformly distributed in the joint FoV of both sensors. The same takes effect for the rotation of the calibration object; it should be recorded with different rotations around all axes [19].

However, the true convergence of the optimization is not ensured, and it finds only a local minimum and not a global minimum. Based on this fact, a threshold was defined from which result of the Levenberg-Marquardt is trusted. Based on several hundred trials, it is recommended, that the calibration and the nonlinear optimization are repeated until the result of the Levenberg-Marquardt minimized distance is less than 2 pixel.

IV. SIMULATION & EXPERIMENT

The simulation and experiments with the real calibration object have been realized to determine the abilities and the performance of the presented approach. In order to allow for a better classification of the simulation results, these were compared against the approaches presented in [10], [18]. Therefore, these simulations were reproduced. Their camera

and LRF parameters are combined with the triangle calibration object in our simulation environment.

During the experiments with the real LRF, differences between the depiction of a scanned object and the real one were identified. These deviations were reduced with the method, as shown in section III. Additionally the experimental results and consequently, the abilities and performances of the presented approach, were compared against the simulation results.

A. Simulation Setup

In order to compare our results with the ones presented in [10], [18], identical constraints, like sensor noise, for VGA and XGA camera, were simulated. The camera's uncertainty is a Gaussian noise, with a mean of 0 and a standard deviation of 0.5 pixels. The noise was added on the calibration triangle corners in the image plane. The simulation of the LRF does not contain a physical engine and the distance measurements are not contaminated with optical effects, like the edge effect. The simulation space contains only the calibration object and, therefore, the identification of this is always unique. Based on this initial situation, no "cleaning" of the distance measurements and no object identification is necessary. Therefore, only the distance measurement was implemented. The LRF was implemented with a uniform noise, whose deviation is 50 mm. This requirement conforms with the ability of our LRF device. The calibration object is an isosceles rectangular triangle without further add-ons because the unique identification can be ensured. The position and the orientation are chosen randomly. The only constraint is that the calibration object appears entirely on the image plane and intersects the LRF plane. In the simulation, the initial parameters were $\phi = [0, 0, 0]^T$ degrees and $t = [0, 0, 0]^T$ meters.

B. Simulation Results

It is shown in [10], [18], that the sample size (size of the data set) of different poses (positions and orientation) of the calibration object has an influence on the calibration result. Figure 4a and 4b show this relation also for the reproduced results of [10], [18] and the results of our approach. The figures show the average scalar translation error and the scalar rotation error, which base on the translation t and rotation ϕ deviation vector between the estimated extrinsic parameters and the ground truth. The showed scalars are the averages of 500 random trails (simulation and experiments). The sample size of poses varies from 6 to 35. The graphs "VGA camera [18]" and "XGA camera [10]" describe the reproduced results of the according approaches. The graph "mean LRF and Sub Pixel" shows the simulation results and "Experiment" depicts the experiment results of our approach. The results of the experiments will be elucidated subsequently in section IV-D. All graphs show that with an increasing number of poses the calibration error decreases. The results of the reproduced approaches show that the translation vector has an average error of $\approx 0.005\,m$ if more than 25 poses are used. These results, as well as the results of the orientation error, reflect the results of the previous works.
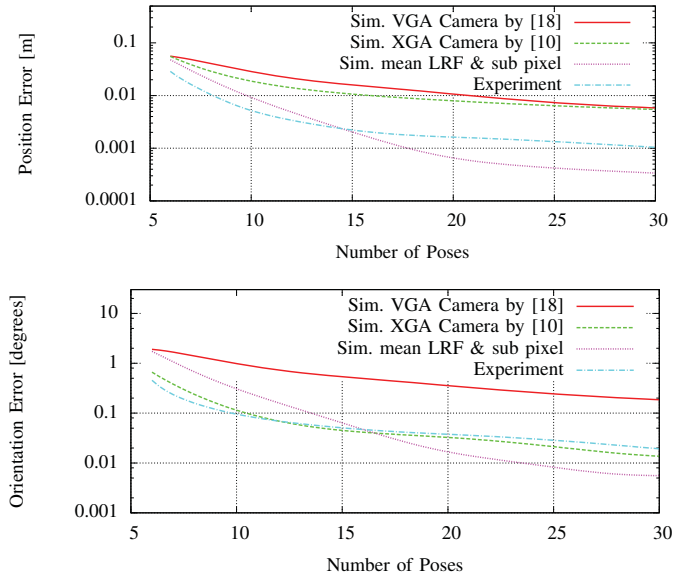

Fig. 4: Position and orientation error vs. the sample size of the calibration object positions and orientations.

Our approach "LRF mean & sub pixel", which use a mean of 10 laser scans and a $\frac{1}{10}$ px sub pixel calculation, achieves with 25 poses a translation error of $\approx 0.0005\,m$. After this point, the accuracy increases only marginally. The achieved orientation error is in the area of $0.008°$, also with 25 poses. Figure 4a shows that an increase of the camera resolution (VGA to XGA) only leads to a marginal reduction for the translation error. In contrast to, the orientation error which substantially increases, by a change from VGA to XGA resolution, as is seen in Figure 4b. If the observation is transferred to our approach, the use of sub pixel calculation has been also only a marginal impact to the translation error, because it is also only an increased resolution. However, the difference between the methods of [10], [18] and our approach is considerable. An explanation can be that the influence of the LRF data accuracy, which was increased also by using a mean of 10 scans, is important for a reduction of the translation error. The further improvement in the submitted approach can be traced back to the increasing of the LRF accuracy.

C. Experimental Set-up

For the assembly of the experiments, a mounting was used where the LRF was combined fixed with the camera, as it can be seen in Figure 1. The LRF device is a Hokuyo UTM-30LX with a $270°$ field of view and $0.25°$ angle resolution [9]. The maximum measurement range is 30 m with an accuracy of $\pm 50\,mm$. The LRF can measure distance and remission values. The camera is a monocular VGA camera.

D. Experimental Results

The surveys of different objects show that the same object in the LRF data has different dimensions, dependent on the measurement method, surface reflectivity and distance to the LRF. An example of this behavior is illustrated in Figure 5, which depicts the remission and distance measurements of an

object with a high reflective surface. The background behind the object is less reflective so that the object is clearly visible in the remission data. The boundaries of the object are represented by D_0 and D_1 in the distance data and R_0 and R_1 in the remission data. The points U_0 and U_1 are the corresponding distance measurements to R_0 and R_1, which means, their angles (polar coordinates) are identical, as is shown in section III. The comparison shows that the distance between D_0 and D_1 is 530 mm, in contrast to 295 mm between U_0 and U_1. The object has a real size of 290 mm and was positioned ≈ 3.8 m in front of the LRF. This is an extreme example, but comparable results were measured with other surfaces like white or black painted wood, too. An explanation for the differences between
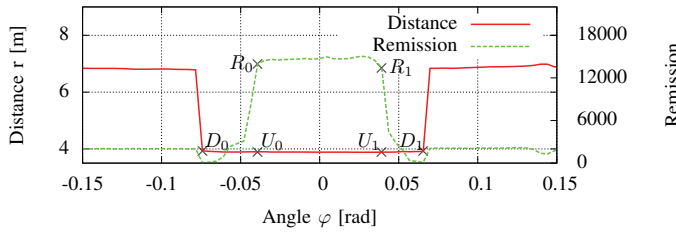

Fig. 5: Survey of an object with distance and remission measurements.

the two measurements methods could be the edge effect. In order to show the relationship between surface remission and the edge effect, it was compared the LRF measurements of four objects, which have different remission values, as is seen in table I. Three of the objects were measured only with distance measurements ("white painted wood", "black painted wood" and "reflector surface"). The fourth "surface with two reflector stripes" was conducted with the procedure which was used for the calibration object, too. In addition to the different surfaces, the influence of the range (1 meter to 5 meters) between the LRF and the test object on the edge effect, was evaluated. The result of the experiment is shown in Figure 6, where the dimension error is depicted against the distance. The dimension error is an average error based on 50 trials at each distance. The pure distance measurements charts show that with increased remission and with increased distance, the dimension error increases, too. In comparison to the results, which were achieved with the pure distance measurements, the dimension error of the combined method is low. Further, the error is relatively constant over the distance. The result of these tests show that not only distance accuracy must be considered during the calibration; also a possible angle error, which is based on the reflectivity of the measured surfaces, has to be considered. In the work of [5] was shown that the surface reflectivity and edge effect have an influence on the accuracy of a LRF distance measurement. A hypothesis is that increasing surface reflectivity leads to increasing edge hits (edge effect). The Hokuyo UTM30LX uses a first echo handling, which uses only the first echo without considering the subsequent echoes. The intensity of an echo depends on the intensity of the spot which hits the surface, and the reflectivity of the hitting surface. Therefore, we assumed that the intensities of the spots, which
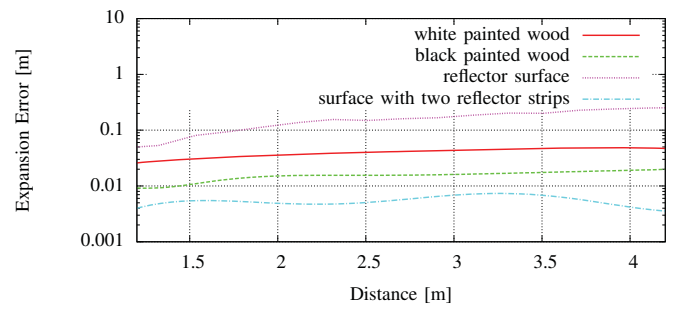

Fig. 6: Survey error of a known object size. The error is depending from the remission level of the object surface.

hit an object, are identical for the same object at a constant range to the LRF. Further it was assumed that an example spot exists, which hits an object edge with less than 100% of its spot profile, and the intensity of the reflected echo is sufficient to enable the detection with the LRF. The resulted measurements of these beams have the same distance value, but a lower remission value (between the points D_0 and U_0 and U_1 and D_1) than a beam, which hits the object with the complete profile (between point U_0 and U_1), as is seen in Figure 5. Based on this observation, we consider that with increasing surface reflectivity the detection of echoes increase, which is based on the edge effect, too. This would explain the observations, as is shown in Figure 3 and 5.

The remission measurements are not influenced by this behavior, as seen in the Figure 6 chart "surface with two reflector strips". Therefore, the proposed calculation with the combination of remission and distance measurements, performs most likely the ground truth dimension of the survey object and, therewith, the assumption of the simulation.

The calibration experiments were conducted in a standard office which was not arranged specially. The positions and the orientations of the proposed calibration object were chosen randomly. The positions ranged from 1 to 4 meters in front of the sensor head, and the only constraint was that the calibration object appears entirely on the image plane and intersects the LRF plane. An example of a corresponding data set, consisting of LRF data and camera data can be seen in Figure 7a and 7b.

The position and orientation errors of this experiment data set is presented in Figure 4a and 4b. They are shown in comparison to the simulation results, as presented in section IV-B. In addition, the position and orientation errors between the computed extrinsic parameters and the ground truth against the sample size of the calibration object poses (size of the initial data set) are shown. Propagated by the simulation, the experimental results show the same tendency. With increasing sample size of the calibration object poses is decrease the position and orientation error. The experimental results are slightly worse than our simulation results. However, the experimental translation error is distinctively less than the simulation results of the methods presented by [10], [18]. The experimental determined orientation error of our approach is comparable with the simulated result of [10]. The experiment achieved
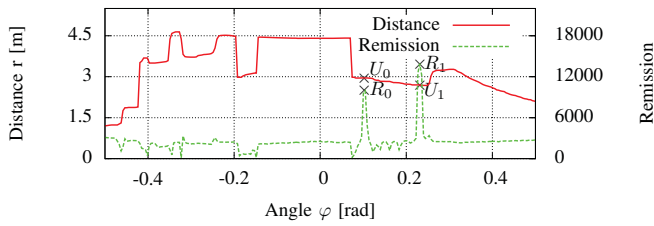
Fig. 7: LRF scan with distance and remission data and gray scaled camera image of the calibration object in an office environment.

a translation error of 1 mm and an orientation error of 0.02 degrees, what is comparable to the results in the work [14]. A resulting projection of the LRF data onto the camera image plane can be seen in figure 8. Causes for the deviations between experiment and simulation results could be the angle error, which was not considered in the simulation, or errors during the identification of the ground truth.
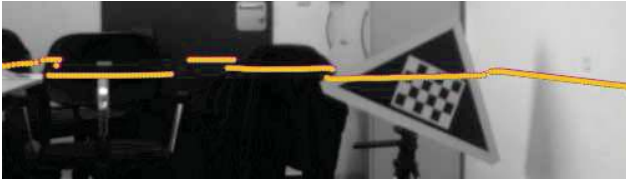

Fig. 8: Projections of the LRF measurements onto the camera image plane using the parameters calibrated by our method.

V. CONCLUSION & FUTURE WORK

In this paper, we presented an automatic extrinsic parameter calibration between a monocular camera and a single line LRF using remission measurements. Therefore was designed a new calibration object which enable a unique identification and more precise survey. For this purpose, the new calibration object was equipped with a significant remission signature which enables a unique identification and a more accurate survey of the calibration object.

The proposed method was validated in simulation and experiment. In order to classify the simulation results, they were compared to existing methods. Thereby, the results show that the proposed method is reliable and more accurate than existing methods. Further, the approach is simple and usable in a variety of environments (indoor/ outdoor).

The calibration of sensor poses in a joint frame enables the fusion of the different sensor data in a single data set, which can be applied to combined environment mapping. The combination of camera and LRF data in a single world model is a topic of the future work. It is anticipated that the combination leads to a more dense resolution or more accurate data than with a single sensor. Further, the combination leads to the

ability to evaluate both sensor solutions against each other (detection of false positives or outliers), which increases the trust in the whole environment mapping.

REFERENCES

[1] Sick lms291 data sheet: Laser measurement technology lms2xx / lms291 / outdoor / mid-range lms291-s05. Waldkirch, 2010.

[2] H. Aliakbarpour, P. Nuez, J. Prado, K. Khoshhal, and J. Dias. An efficient algorithm for extrinsic calibration between a 3d laser range finder and a stereo camera for surveillance. In *Advanced Robotics 2009 ICAR 2009 ICAR 2009. International Conference on*, page 16.

[3] H. Baltzakis, A. Argyros, and P. Trahanias. Fusion of range and visual data for the extraction of scene structure information. In *Pattern Recognition, 2002. Proceedings. 16th International Conference on*, volume 4, page 711, 2002.

[4] D. Bi and X. Lu. A new flexible approach for single laser stripe profiler calibration. *IEEEProceedings on Information and Automation*, page 7680, 2008.

[5] W. Boehler, Bordas M. Vicent, and A. Marbs. Investigating laser scanner accuracy. In *Proceedings of XIXth CIPA International Symposium*, 2003.

[6] Eric K. Forkuo and Bruce King. Automatic fusion of photogrammetric imagery and laser scanner point clouds. In *In International Archives of Photogrammetry and Remote Sensing, vol. XXXV, part B4*, pages 921–926, 2005.

[7] Simone Frintrop, Erich Rome, Andreas Nchter, and Hartmut Surmann. An attentive, multi-modal laser "eye". In *Proc. of 3rd Intl Conf. on Computer Vision Systems (ICVS 2003*, pages 202–211. Springer, 2003.

[8] J.L.L Galilea, J.-M Lavest, C.A.L Vazquez, A. Gardel Vicente, and I. Bravo Munoz. Calibration of a high-accuracy 3-d coordinate measurement sensor based on laser beam and cmos camera. *Instrumentation and Measurement, IEEE Transactions on*, 58(9):3341–3346, 2009.

[9] HOKUYO AUTOMATIC. Scanning laser range finder utm-30lx/ln specification. Japan.

[10] Ganhua Li, Yunhui Liu, Li Dong, Xuanping Cai, and Dongxiang Zhou. An algorithm for extrinsic parameters calibration of a camera and a laser range finder using line features. In *Intelligent Robots and Systems, 2007. IROS 2007. IEEE/RSJ International Conference on*, pages 3854–3859, 2007.

[11] C. Mei and P. Rives. Calibration between a central catadioptric camera and a laser range finder for robotic applications. In *Robotics and Automation, 2006. ICRA 2006. Proceedings 2006 IEEE International Conference on*, pages 532–537.

[12] J. Miura, Y. Negishi, and Y. Shirai. Mobile robot map generation by integrating omnidirectional stereo and laser range finder. In *Intelligent Robots and System, 2002. IEEE/RSJ International Conference on Proceedings*, volume 1, pages 250–255. IEEE Operations Center, 2002.

[13] P. Moghadam, W. S. Wijesoma, and Jun Feng Dong. Improving path planning and mapping based on stereo vision and lidar. In *Control, Automation, Robotics and Vision, 2008. ICARCV 2008. 10th International Conference on*, pages 384–389, 2008.

[14] O. Naroditsky, A. Patterson, and K. Daniilidis. Automatic alignment of a camera with a line scan lidar system. In *Robotics and Automation (ICRA), 2011 IEEE International Conference on*, pages 3429–3434, 2011.

[15] J. Santolaria, J. J. Pastor, F. J. Brosed, and J. J. Aguilar. A one-step intrinsic and extrinsic calibration method for laser line scanner operation in coordinate measuring machines. *Measurement Science and Technology*, (20), 2009.

[16] D. Scaramuzza, A. Harati, and R. Siegwart. Extrinsic self calibration of a camera and a 3d laser range finder from natural scenes. In *Intelligent Robots and Systems, 2007. IROS 2007. IEEE/RSJ International Conference on*, pages 4164–4169, 2007.

[17] K.M Wurm, R. Kummerle, C. Stachniss, and W. Burgard. Improving robot navigation in structured outdoor environments by identifying vegetation from laser data. In *Intelligent Robots and Systems, 2009. IROS 2009. IEEE/RSJ International Conference on*, pages 1217–1222, 2009.

[18] Qilong Zhang and Robert Pless. Extrinsic calibration of a camera and laser range finder (improves camera calibration). 3:2301 – 2306, 2004.

[19] Z. Zhang. A flexible new technique for camera calibration. *Pattern Analysis and Machine Intelligence, IEEE Transactions on*, 22(11):1330–1334, 2000.